LETTER

Effect of tissue staining in quantitative phase imaging

Sungbea Ban[1] | Eunjung Min[2] | Yujin Ahn[1] | Gabriel Popescu[3]* | Woonggyu Jung[1]*

[1]Department of Biomedical Engineering, Ulsan National Institute of Science and Technology (UNIST), Ulsan, Republic of Korea

[2]Rowland Institute at Harvard University, Cambridge, Massachusetts

[3]Quantitative Light Imaging Laboratory, Department of Electrical and Computer Engineering, Beckman Institute for Advanced Science and Technology, University of Illinois at Urbana-Champaign, Urbana, Illinois

*Correspondence

Gabriel Popescu, Quantitative Light Imaging Laboratory, Department of Electrical and Computer Engineering, Beckman Institute for Advanced Science and Technology, University of Illinois at Urbana-Champaign, Urbana, IL.
Email: gpopescu@illinois.edu
Woonggyu Jung, Department of Biomedical Engineering, Ulsan National Institute of Science and Technology (UNIST), Ulsan, Republic of Korea.
Email: wgjung@unist.ac.kr

Quantitative phase imaging (QPI) is an emerging modality, which enables the identification of abnormalities in tissue based on optical properties. QPI can be applied to any biological specimen due to its label-free imaging capability, but its use in stained tissue is unclear. Here, we study the variability of QPI with the staining dye. Several tissues such as brain, heart and lung were stained with hematoxylin and eosin, and their optical properties compared at 550 and 730 nm. Our results showed that phase and scattering coefficients varied when QPI was used at the absorption wavelength of the staining dye. We also found that the variation of optical properties was dependent on tissue morphology.
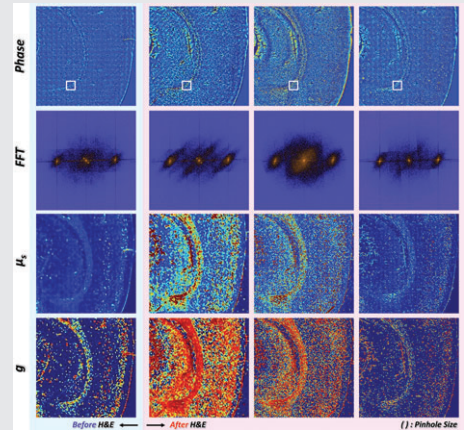
1 | INTRODUCTION

The histological examination of tissue is the gold standard for studying its morphology and abnormalities [1]. In order to visualize the structural details of specimens using bright field microscopy, labor and time intensive procedures for histologic preparation are required, including staining. Hematoxylin and eosin (H&E) staining is commonly used in histopathology as it can present strong contrast of cytoplasm and nucleus, and enable the diagnosis of many conditions. Although histological observation has been widely used in various biological studies and has a long history, it lacks of quantitative analysis, and its yield varies depending on the ability of the operator. Furthermore, variability in tissue properties owing to different staining protocol and the pathologist's training result in inter-observer disagreement [1]. To overcome these limitations, there is a significant need for alternative techniques, which are stain-independent, high-throughput and quantitative. Advanced optical imaging techniques developed over the last decade have provided various contrast modal

ities in histopathology, with high sensitivity, resolution and speed. Among them, quantitative phase imaging (QPI) is the 1 promising technique. QPI provides quantitative information about the structure of a specimen with nano-scale sensitivity, without the need for staining and labeling [2, 3]. Since it is also suitable to integrate into a conventional microscopy platform, it has been actively investigated as a means of visualizing the abnormality of various cells and tissues [4–16]. Although QPI has unique advantages and potential for the study of histopathology, most research has been focused on cellular level studies or tissue analysis with a limited field of view [17–23].

Recently, the application of QPI on large-scale tissue has received increased attention. Several studies measured the refractive index (RI) and scattering parameters of tissue abnormalities in, for example, various tissue cancer model, renal injury, and Alzheimer's disease [24–30]. Since histological examination of tissues has been the routine procedure in pathology, QPI must be tested against this established method. In particular, the study of differences in QPI before and after staining tissues is essential, considering the absorption of staining molecules and affinity to the specimens, which induce RI changes. However, there has been a lack of investigation into the effects of staining, despite a clear and practical need.

In this study, we developed a home-built diffraction phase microscope (DPM) [2], which enables the wide-field and label-free visualization of various tissues. In order to address the aforementioned question, we investigated the optical properties revealed by QPI in unstained vs stained tissues.

2 | MATERIALS AND METHODS

2.1 | Wide-field diffraction phase microscopy system

The experimental setup is depicted in Figure 1. The DPM is based on a single shot, off-axis common path geometry equipped with a long travel motorized XY stage (MT mot 100×100 MR, Märzhäuser Wetzlar, Wetzlar, Germany). Two spatially coherent visible continuous wave laser source (CW) lasers with center wavelengths of 550 nm (CW Visible, MPB Communications Inc., Pointe-Claire, Canada) and 730 nm (OBIS 730LX, Coherent, USA) are used as light sources. Light is launched and spatially filtered by a pinhole (P1) to produce a clean Gaussian beam. The scattered light from the bio-specimen is collected by an objective lens (UMPlanFL 40× NA 0.8, Olympus, Tokyo, Japan). Diffraction grating (92 grooves/mm, Edmund

Optics, USA) is placed at the image plane (IP) to generate multiple diffraction orders. The zeroth beam is low-pass filtered by the pinhole (P2) on the Fourier plane (FP), which plays the role of a reference field. The first order beam is completely passed without any field interruption, which is used as the sample field. The detailed description of the pinhole is illustrated in Figure 1, where the diameter of the pinhole is shown to be 50 μm. The alignment of lenses L5 and L6 forms a highly stable Mach-Zehender interferometer, and the spatially modulated interferogram is captured by a electron multiplying charged coupled device (EMCCD) (iXon3, Andor, Northern Ireland) with high sensitivity.

The phase delay $\varphi(r)$ from the measured interferogram can be retrieved by simple band-pass filtering in the Fourier domain, which results to a Hilbert transform [31, 32].

$$\varphi(r) = \arg\left[\left\langle U_s^*(r,t)U_r(r,t)\right\rangle_t\right] \approx \arg\left[\left\langle U_i^*(r,t)U_i(r,t)e^{i\varphi(r)}\right\rangle_t\right]. \quad (1)$$

U_i is an incident optical field assuming that U_r gets closer to $U_i(r, t)$ after light passes through the pinhole, which can be expressed as $U_s(r, t) * h(r) \approx U_i(r, t)$. Where, $h(r)$ denotes the circular aperture function of the pinhole. Using field-retrieval algorithm [30], spatially modulated first-order after Fourier transform of raw interferogram was selected by band-pass filter and shifted back to baseband. In order to measure the phase distortion caused by optics and aperture in the system, calibrated image complex field was acquired in the no-sample region [19, 33]. And, the background subtracted clean phase image was produced by the division of image complex field and calibrated image complex field. Since every image was affected by the same distortion, by applying this simple procedure to every image, we had clear stitching result. The transverse resolution was 1.3 μm at the center wavelength of 550 nm, and acquisition time was 100 frames/s. The phase spatial and temporal sensitivity of the system were measured to be 50 and 60 mrad,
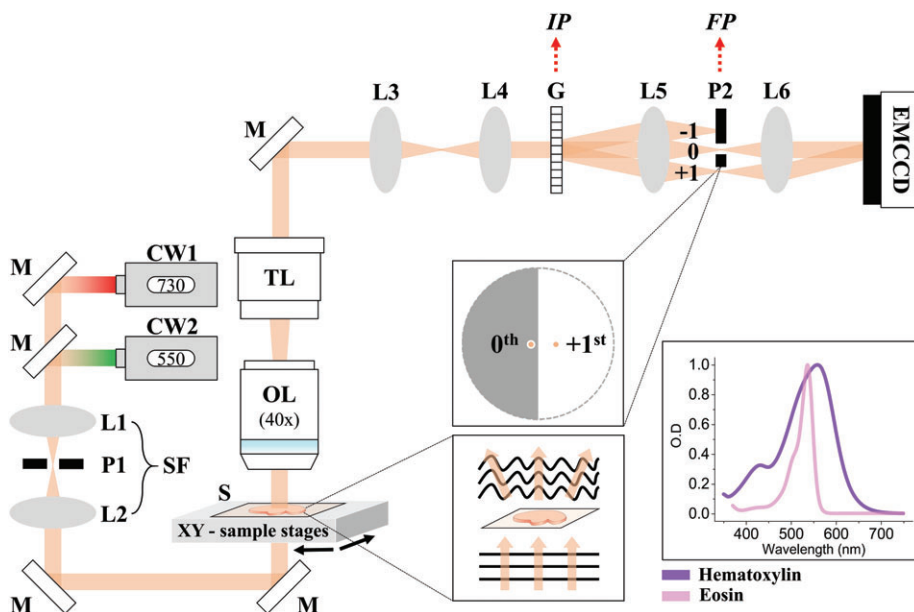

FIGURE 1 Schematics of home-built wide-field DPM. M, mirror; L, lens; CW, continuous wave laser source; TL, tube lens; OL, objective lens; G, diffraction grating; P, pinhole; EMCCD, electron multiplying charged coupled device; S, sample; IP, image plane; FP, Fourier plane; SF, spatial filter. Optical absorption spectrum of H&E dye is presented right corner. Focal length of lens: L1-2 ($f = 100$ mm), TL ($f = 200$ mm), L3 ($f = 150$ mm), L4 ($f = 35$ mm), L5 ($f = 40$ mm) and L6 ($f = 200$ mm)

respectively. OCT imaging system is automatically operated by home-built LabVIEW software.

2.2 | Animal sample preparation

In this experiment, DPM image-sets from the coronal section of a brain, heart and lung were acquired. For the preparation of various mouse tissues, we used 8-week-old wild-type male mice. Every tissue went through a paraffin infiltration process. Then, dehydrated tissue samples were embedded in paraffin and sectioned along the coronal plane with a thickness of 5 μm using a microtome (RM2255, Leica Microsystems, Germany). Prior to imaging, the paraffin was completely removed by washing it away with xylene and a series of graded ethanol solutions. For QPI imaging, the deparaffinized tissue is mounted on the slide glass and cover slipped. For H&E staining, deparaffinized tissue is stained by H&E dye through conventional staining protocol, then rinsed out with running tap water. The optical absorption spectrum of H&E was also measured by spectrophotometer (Cary 5000, Agilent, USA) which was illustrated in Figure 1. All procedures of sample preparation in this study, including animal experiments, were carried out in tight accordance with the approved guidelines of Institutional Animal Care and Use Committee at Ulsan National Institute of Science and Technology (UNISTIACUC-17-07).

3 | RESULTS AND DISCUSSION

3.1 | Wide-field DPM imaging in animal tissue slice

To achieve the wide-field DPM image, each type of mouse tissue sliced into 5 μm thick were mounted on the XY stage and imaged using the pairwise mosaic technique. We acquired respectively brain, lung and heart tissue, 442, 315 and 337 single DPM images. The FOV of a single image was $150 \times 150 \ \mu m^2$, and the overlapping ratio between 2 adjacent images was 25%. Figure 2 shows wide-field images of mouse brain tissue. Figure 2A shows a QPI image of sliced brain tissue without staining at 550 nm wavelength. The QPI image delineates the detailed brain structure such as cerebral cortex, caudate putamen, and corpus callosum (CC). The CC region has a higher phase delay than the other regions due to a high RI of the lipid component. A region of CC is denoted by a white box and its Fourier transform (FFT) is presented at the bottom in Figure 2A. For accurate comparison, the same brain tissue went through the H&E staining process and imaged by bright field microscopy as shown in Figure 2B. Our results show that the morphology of brain tissue acquired from QPI and histological imaging has a strong correlation under the same magnification of objective lens (×40).
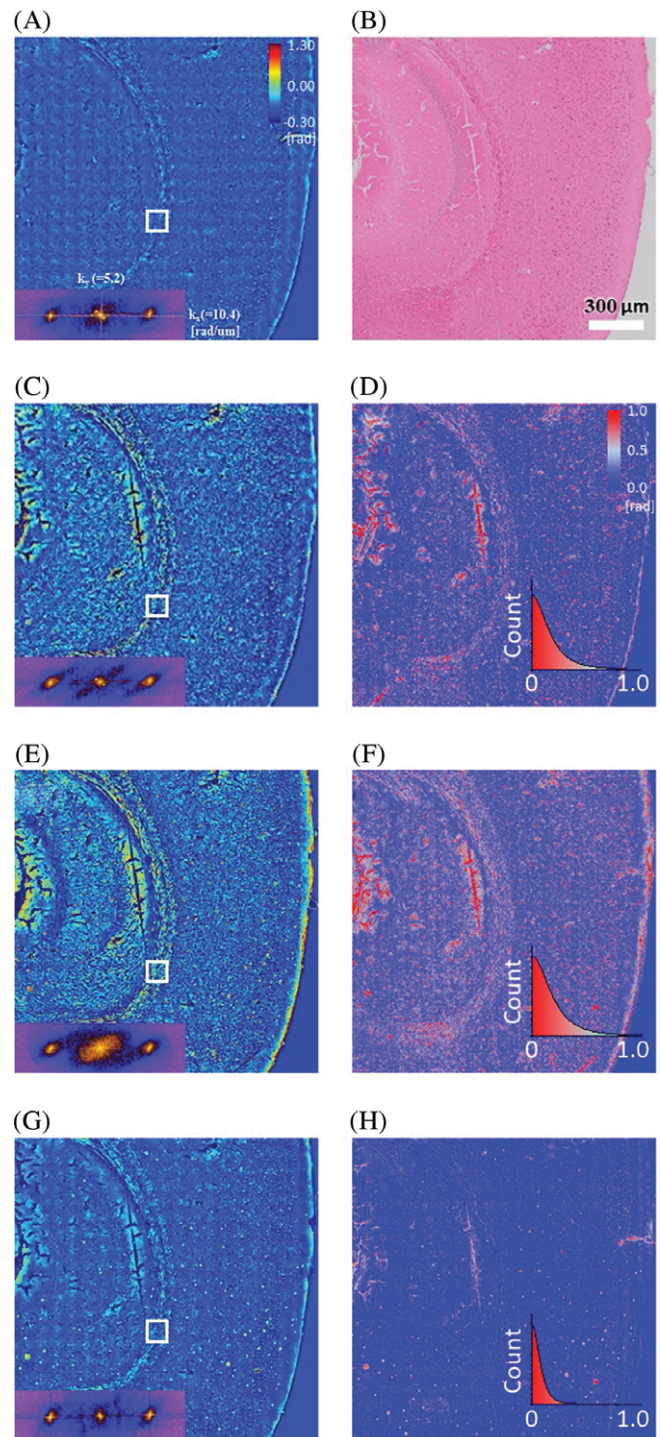

FIGURE 2 Wide-field DPM images of a mouse brain tissue slice before and after H&E staining. (A) Phase delay map of raw brain slice image using 550 nm CW laser. (B) Bright field image of same tissue slice stained by H&E. (C) Phase delay map measured with 550 nm CW laser after H&E staining. (D) Phase delay difference obtained by subtracting (A) from (C). (E) Phase delay map after H&E stained using 550 nm CW laser with smaller pinhole of 20 μm diameter. (F) Phase subtraction of (A) from (E). (G) Phase delay map measured with 730 nm CW laser after H&E staining. (H) Phase subtraction of (A) from (G). The insets in phase delay maps are scattering wave vector map for the region of CC. Histogram counts each pixel value from the phase subtraction. Scale bar: 300 μm. In the tissue handling process, physical deformation induced unintended alteration of phase delay near the perimeter of the brain tissue
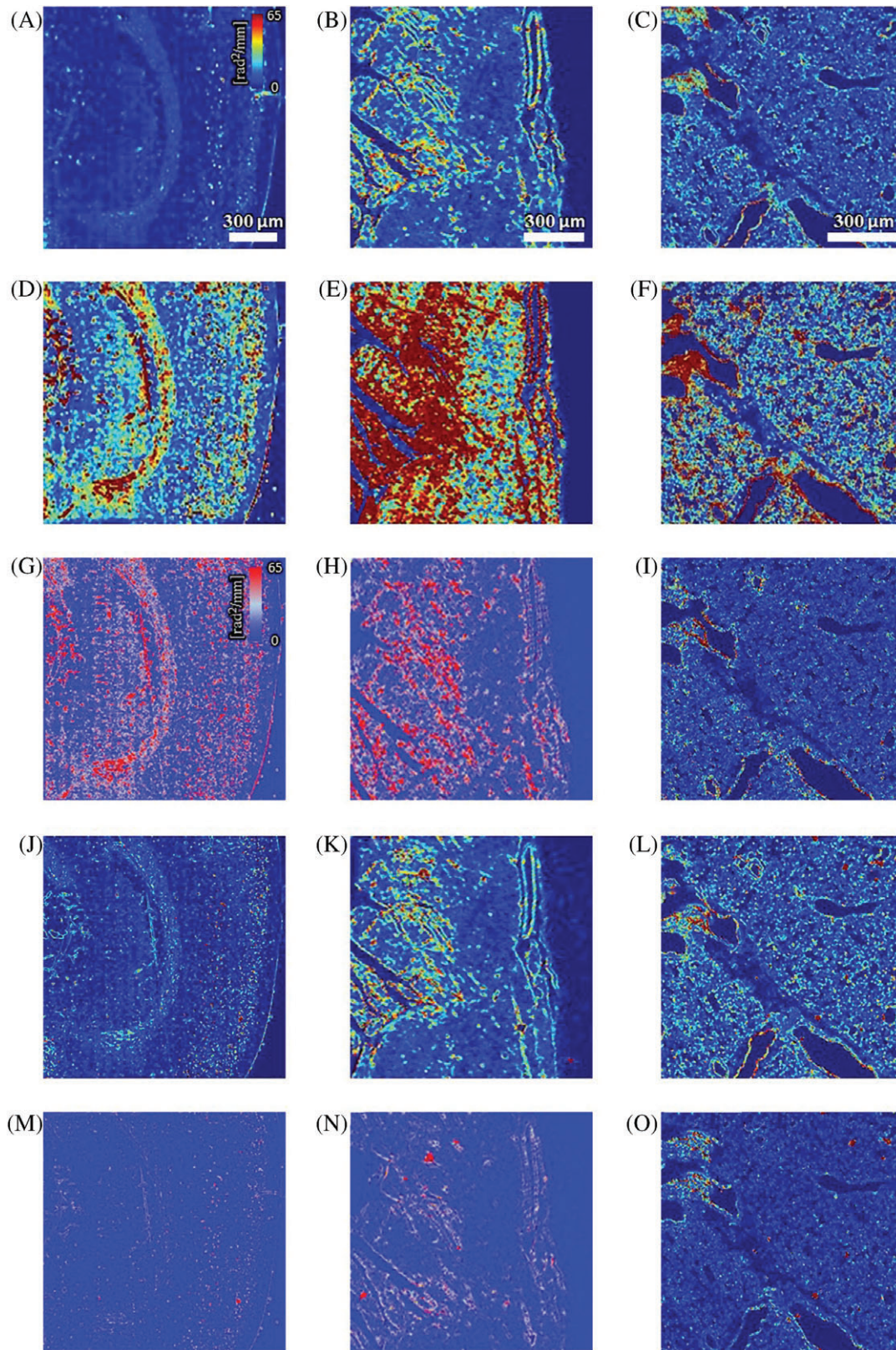
FIGURE 3 Scattering coefficient map (μ_s) of brain, heart and lung tissue slices obtained from the wide-field DPM. (A) μ_s map of unstained brain slice imaged using 550 nm. (B) μ_s map of H&E stained same brain slice imaged using 550 nm. (C) μ_s difference between (A) and (B). (D) μ_s map of H&E stained same brain slice imaged using 730 nm. (E) μ_s difference between (A) and (D). Same approaches were applied for heart (F-J) and lung (K-O). Scale bar: 300 μm

Since the staining can be highly expected to influence the RI of the investigated tissues, we also calculated the RI of unstained tissue from the detected quantitative phase images. Phase delay is achieved by the difference of RI and thickness of tissue slice, thus the actual value of RI can be retrieved by the following manner:

$$RI\,(n) = \frac{\varnothing}{2*pi} * \frac{\lambda}{h} + n_{m,} \qquad (2)$$

where lambda is the light wavelength, and h is thickness of sliced tissue (5 μm), n_m is RI of mounting agent. It is found that unstained tissues of brain, heart and lung have the average value of 1.376, 1.392 and 1.365, respectively.

To investigate the effect of staining (Figure 2C), we then measured the phase delay in H&E stained brain slices with a 550 nm laser. We found that the phase delay and its variation value changed because the phase is altered by intensity modulation caused by complex of absorption and structural alteration due to staining molecules. Specifically, the relation between absorption and RI can be explained via the Kramers-Kronig relationship [34]. The key idea is that the change in the RI is related to the change in the absorption. Thus, in high absorption vs transparent areas (low absorption), the tissue will exhibit different RI as well. If the measurement frequency is closer to the absorption band, one can indicate that the high-absorption species (H&E staining molecules) is associated with higher RI, while non-stained molecules maintains their RI. Due to the altered phase term by this phenomenon, thus, the intensity modulation also clearly appears in the Fourier domain of the power spectrum, as shown in the inset of Figure 2C. The angular scattering components are spread into the higher frequency region compare to Figure 2A. The phase subtraction of Figure 2A from Figure 2C is presented in Figure 2D, and illustrates significant phase difference before and after H&E staining.

3.2 | Phase distortion due to absorption of staining molecules and structural alteration

There is a possibility, however, that the intensity modulation could be created from insufficient spatial filtering in the reference field. The inappropriate spatial filtering makes a spatially non-uniform field and might provide incorrect phase value. Hence, we replaced the 50 μm diameter pinhole with a 20 μm pinhole, from which the result is demonstrated in Figure 2E. Although we reduced the pinhole size by more than half, the result is not significantly different from that in Figure 2D. That is, the incorrect phase did not originate from the spatially incoherent reference field, but from inherent absorption based phase modulation due to staining dye.

To recover the original phase delay before the H&E staining, the simple but effective solution was to apply a light source that had different spectral bands avoiding the absorption range (400–700 nm) of the staining dyes. We used the 730 nm CW laser instead of 550 nm, and a pinhole of 50 μm diameter. With a 730 nm light source, the result was similar to those obtained when an unstained brain slice was imaged using 550 nm, as shown in Figure 2G. The phase subtraction gives much lower values compared to the previous 2 subtraction images, as in Figure 2H.
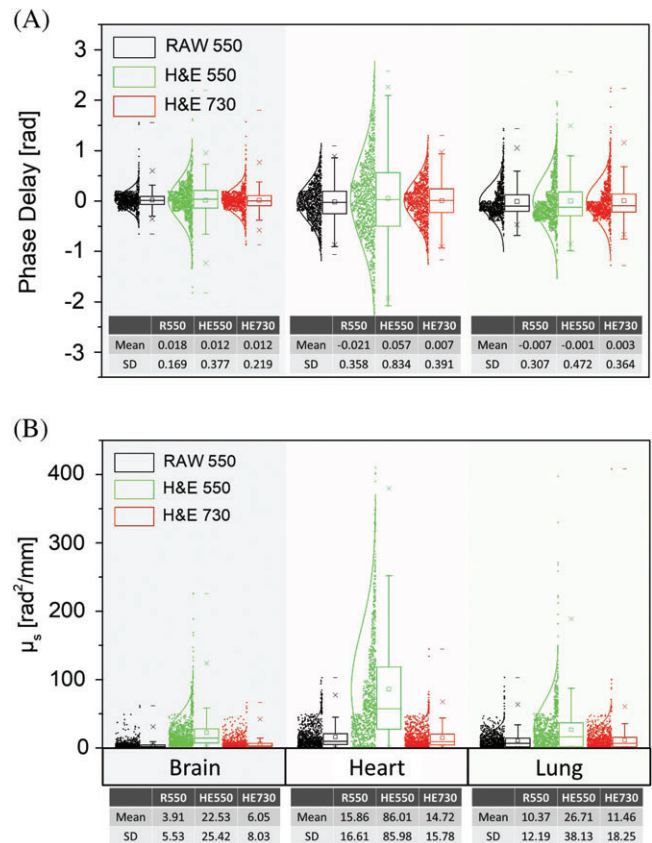

FIGURE 4 Quantitative analysis of phase delay and scattering parameters in brain, heart and lung. Each different color bar indicates different experimental conditions in phase measurement. (A) Distributions of phase delay in brain, heart, and lung. (B) Distributions of scattering coefficient calculated from phase variance. Mean and SD are abbreviations of average value of each parameter and SD, respectively

Since we successfully obtained phase delay independent of H&E staining, we were able to compare the optical properties of a tissue slice before and after the staining. The scattering coefficient ($μ_s$) was calculated using the measured phase information according to the scattering-phase theorem [35]. In general, light attenuation is measured with respect to the depth of sample and converted to a scattering coefficient based on the Beer-Lambert law. However, the scattering-phase theorem can calculate the scattering coefficient with only a 2D phase image in the following manner:

$$\mu_s = \frac{\langle \Delta\varphi^2(r) \rangle_r}{L}, \qquad (3)$$

where indicates spatial variance in the phase image and L is the thickness of the tissue slice, 5 μm in this case. Thus, the optical properties can be obtained using the phase variance in a spatially resolved manner [35]. The window size for the calculation was 3.0×3.0 μm². According to the scattering-phase theorem, the scattering coefficient is proportional to the phase variance, meaning the increase of scattering at high-phase fluctuation. Also, since we use very thin tissue slices (5 μm) in our measurement, which means that we are in the single scattering regime (the mean free path is

much longer than the thickness of the tissue slice) [35]. Therefore, the absorption and, thus, dispersion is not significant.

Figure 3A,B is μ_s maps retrieved by 550 nm illumination source for unstained and H&E stained brain slice in turn. Compared to Figure 3A,B shows higher phase variance over the entire area due to high-power fluctuation induced by absorption of H&E. On the other hand, the phase variance obtained at 730 nm wavelength remains similar to that before staining (Figure 3D). Figure 3C,E represents the μ_s difference based on subtraction from unstained mouse bran slice at 2 different wavelength of each 550 and 730 nm. The same approach toward different tissues of heart and lung is presented in Figure 3F-J and K-O, respectively. The quantitative analysis of phase delay and scattering coefficient corresponding to Figure 3 was performed, as shown in Figure 4. In every tissue sample, high-phase variation was detected in stained tissue at 550 nm wavelength. We also found that heart tissue induced a relatively high-phase fluctuation compared to brain and lung tissues. This is because of the contractile structure of cardiac muscle tissue. Since the cardiac muscle tissue is made of many densely packed myocardiocytes and fibers, it exhibits much higher phase variance after staining. Since phase variance is proportional to the scattering coefficient according to scattering-phase theorem, the broad distribution of the phase value in heart tissue corresponds to the high-scattering coefficient as in Figure 4B. In Figure 4B, scattering coefficient values in every stained tissue generally increase when illuminated by 550 nm but immediately revert to the original value when illuminated by 730 nm.

4 | CONCLUSION

In summary, we developed a wide-field DPM, which can render not only multi-scale morphological information of tissue slices, but also their optical characteristics. In order to verify the influence of H&E staining in terms of phase delay and optical properties, 3 different types of mouse tissue were imaged and quantitatively analyzed. The phase delay and scattering coefficient in stained tissue significantly increase when the illumination source was used in the absorption range of the H&E dye. On the other hand, the effect of staining was negligible when using a light source out of the absorption spectrum. We also found that the variation of optical properties is also dependent on tissue structure. In particular, the heart, which showed high-phase variance due to its physical composition of densely packed cardiomyocytes and muscle fibers, exhibited a high-scattering coefficient. In the case of brain tissue, phase fluctuation was relatively low and corresponding μ_s had less value except in the region where many lipid components are located such as the CC. Our experimental results show that QPI can be a

quantitative tool in histopathology of both stained and unstained tissues.

ORCID

Sungbea Ban 🔟 http://orcid.org/0000-0002-6165-824X

Yujin Ahn 🔟 http://orcid.org/0000-0002-4383-8773

Woonggyu Jung 🔟 http://orcid.org/0000-0001-7424-3679

REFERENCES

[1] V. Kumar, A. K. Abbas, J. C. Aster, S. L. Robbins, *Robbins Basic Pathology*, Elsevier Saunders, Amsterdam, **2013**.

[2] B. Bhaduri, C. Edwards, H. Pham, R. J. Zhou, T. H. Nguyen, L. L. Goddard, G. Popescu, *Adv. Opt. Photonics* **2014**, *6*, 57.

[3] G. Popescu, *Quantitative Phase Imaging of Cells and Tissues*, McGraw-Hill, New York, NY **2011**.

[4] M. G. Shan, M. E. Kandel, G. Popescu, *Opt. Express* **2017**, *25*, 1573.

[5] E. J. Min, S. B. Ban, Y. Y. Wang, S. C. Bae, G. Popescu, C. Best-Popescu, W. G. Jung, *Biomed. Opt. Express* **2017**, *8*, 1763.

[6] E. Min, M. E. Kandel, C. J. Ko, G. Popescu, W. Jung, C. Best-Popescu, *Sci. Rep.* **2016**, 6, 39667.

[7] G. Di Caprio, M. A. Gioffre, N. Saffioti, S. Grilli, P. Ferraro, R. Puglisi, D. Balduzzi, A. Galli, G. Coppola, *IEEE J. Sel. Top. Quantum Electron.* **2010**, *16*, 833.

[8] F. Merola, L. Miccio, P. Memmolo, G. Di Caprio, A. Galli, R. Puglisi, D. Balduzzi, G. Coppola, P. Netti, P. Ferraro, *Lab. Chip* **2013**, *13*, 4512.

[9] G. Coppola, G. Di Caprio, M. Wilding, P. Ferraro, G. Esposito, L. Di Matteo, R. Dale, G. Coppola, B. Dale, *Zygote* **2014**, *22*, 446.

[10] P. Memmolo, G. Di Caprio, C. Distante, M. Paturzo, R. Puglisi, D. Balduzzi, A. Galli, G. Coppola, P. Ferraro, *Opt. Express* **2011**, *19*, 23215.

[11] P. Memmolo, M. Iannone, M. Ventre, P. A. Netti, A. Finizio, M. Paturzo, P. Ferraro, *Opt. Express* **2012**, *20*, 28485.

[12] P. Memmolo, L. Miccio, A. Finizio, P. A. Netti, P. Ferraro, *Opt. Lett.* **2014**, *39*, 2759.

[13] B. Kemper, G. von Bally, *Appl. Opt.* **2008**, *47*, A52.

[14] M. K. Kim, *Principles and Techniques of Digital Holographic Microscopy*, Vol. 1, SPIE, California, USA, **2010**, p. 51.

[15] K. Lee, K. Kim, J. Jung, J. Heo, S. Cho, S. Lee, G. Chang, Y. Jo, H. Park, Y. Park, *Sensors (Basel)* **2013**, *13*, 4170.

[16] P. Marquet, C. Depeursinge, P. J. Magistretti, *Neurophotonics* **2014**, *1*, 020901.

[17] A. A. Evans, B. Bhaduri, G. Popescu, A. J. Levine, *Proc. Natl. Acad. Sci. U.S.A.* **2017**, *114*, 2865.

[18] G. Popescu, Y. Park, N. Lue, C. Best-Popescu, L. Deflores, R. R. Dasari, M. S. Feld, K. Badizadegan, *Am. J. Phys. Cell Phys.* **2008**, *295*, C538.

[19] H. V. Pham, C. Edwards, L. L. Goddard, G. Popescu, *Appl. Opt.* **2013**, *52*, A97.

[20] G. Popescu, L. P. Deflores, J. C. Vaughan, K. Badizadegan, H. Iwai, R. R. Dasari, M. S. Feld, *Opt. Lett.* **2004**, *29*, 2503.

[21] X. Mo, B. Kemper, P. Langehanenberg, A. Vollmer, J. Xie, G. V. Bally, *Application of Color Digital Holographic Microscopy for Analysis of Stained Tissue Sections*, Vol. 7367, SPIE, California, USA, **2009**, p. 6.

[22] P. Lenz, D. Bettenworth, P. Krausewitz, M. Bruckner, S. Ketelhut, G. von Bally, D. Domagk, B. Kemper, *Integr. Biol. (Camb)* **2013**, *5*, 624.

[23] D. Bettenworth, A. Bokemeyer, C. Poremba, N. S. Ding, S. Ketelhut, P. Lenz, B. Kemper, *Histol. Histopathol.* **2017**, *33*, 11937.

[24] M. E. Kandel, S. Sridharan, J. Liang, Z. Luo, K. Han, V. Macias, A. Shah, R. Patel, K. Tangella, A. Kajdacsy-Balla, G. Guzman, G. Popescu, *J. Biomed. Opt.* **2017**, *22*, 66016.

[25] M. Lee, E. Lee, J. Jung, H. Yu, K. Kim, J. Yoon, S. Lee, Y. Jeong, Y. Park, *Sci. Rep.* **2016**, *6*, 31034.

[26] S. Sridharan, V. Macias, K. Tangella, A. Kajdacsy-Balla, G. Popescu, *Sci. Rep.* **2015**, *5*, 9976.

[27] P. Wang, R. Bista, R. Bhargava, R. E. Brand, Y. Liu, *Opt. Lett.* **2010**, *35*, 2840.

[28] Z. Wang, K. Tangella, A. Balla, G. Popescu, *J. Biomed. Opt.* **2011**, *16*, 116017.

[29] S. Ban, E. Min, S. Baek, H. M. Kwon, G. Popescu, W. Jung, *Biomed. Opt. Express* **2018**, *9*, 921.

[30] P. Wang, R. K. Bista, W. E. Khalbuss, W. Qiu, S. Uttam, K. Staton, L. Zhang, T. A. Brentnall, R. E. Brand, Y. Liu, *J. Biomed. Opt.* **2010**, *15*, 066028.

[31] G. Popescu, T. Ikeda, R. R. Dasari, M. S. Feld, *Opt. Lett.* **2006**, *31*, 775.

[32] Y. Jang, J. Jang, Y. Park, *Opt. Express* **2012**, *20*, 9673.

[33] C. Edwards, A. Arbabi, G. Popescu, L. L. Goddard, *Light Sci. Appl.* **2012**, *1*, e30.

[34] C. C. Wu, T. M. Liu, T. Y. Wei, L. Xin, Y. C. Li, L. S. Lee, C. K. Chang, J. L. Tang, S. S. Yang, T. H. Wei, *Opt. Express* **2010**, *18*, 22637.

[35] Z. Wang, H. Ding, G. Popescu, *Opt. Lett.* **2011**, *36*, 1215.